GEOPHYSICAL RESEARCH LETTERS

Supporting Information for "The role of sediment subduction and buoyancy on subduction dynamics and geometry"

S. Brizzi[1], T.W. Becker[1], C. Faccenna[1,2], W. Behr[3], I. van Zelst[4], L. Dal Zilio[5], Y. van Dinther[6]

[1]Jackson School of Geosciences, The University of Texas at Austin, Austin, TX, USA

[2]Laboratory of Experimental Tectonics, University of Roma Tre, Rome, Italy

[3]Department of Earth Science, ETH Zürich, Zürich, Switzerland

[4]Institute of Geophysics and Tectonics, School of Earth and Environment, University of Leeds, Leeds, UK

[5]Seismological Laboratory, California Institute of Technology, Pasadena, CA, USA

[6]Department of Earth Sciences, Utrecht University, Utrecht, The Netherlands

Contents of this file

1. Text S1 to S2
2. Figures S1 to S5
3. Table S1

Text S1. Numerical method

We use the two-dimensional, continuum, visco-elasto-plastic, seismo-thermo-mechanical version (van Dinther et al., 2013) of the code I2ELVIS (Gerya & Yuen, 2007), which uses an implicit, conservative finite difference scheme on a fully staggered Eulerian grid in combination with a Lagrangian marker-in-cell technique.

The code solves for the conservation of mass, momentum and energy with a visco-elasto-plastic rheology. Lagrangian markers advect physical properties (e.g., viscosity, stress, plastic strain, and temperature) according to the velocity field interpolated from the Eulerian grid (Gerya & Yuen, 2007).

The continuity (Eq. 1), and momentum (Eq. 2 – 3) equations are solved to obtain the horizontal and vertical components of velocity, v_x and v_z, and pressure P (defined as mean stress):

$$\frac{\partial v_x}{\partial x} + \frac{\partial v_z}{\partial z} = 0, \tag{1}$$

$$\frac{\partial \sigma'_{xx}}{\partial x} + \frac{\partial \sigma'_{xz}}{\partial z} - \frac{\partial P}{\partial x} = \rho \frac{D v_x}{Dt}, \tag{2}$$

$$\frac{\partial \sigma'_{zx}}{\partial x} + \frac{\partial \sigma'_{zz}}{\partial z} - \frac{\partial P}{\partial z} = \rho \frac{D v_z}{Dt} - \rho g, \tag{3}$$

where ρ is density, σ'_{ij} are the deviatoric stress tensor components, and $g = 9.8$ m/s^2 is the gravitational acceleration.

The continuity equation (Eq. 1) assumes an incompressible medium, i.e., Poisson's ratio $\nu = 0.5$. The momentum equations (Eq. 2 – 3) include an inertial term that is negligible during long-term subduction. The energy equation (Eq. 4) is solved for the temperature T:

$$\rho C_p\left(\frac{DT}{Dt}\right) = -\frac{\partial q_x}{\partial x} - \frac{\partial q_z}{\partial z} + H_a + H_s + H_r \tag{4}$$

where C_p is the isobaric heat capacity, q_x and q_z are the horizontal and vertical heat flux, H_a is the internal heat generation due to adiabatic (de)compression, H_s is the shear heating due to anelastic deformation, and H_r is the radioactive heat production. q_x, q_z, H_s, and H_a are defined as follows:

$$q_x = -k\frac{\partial T}{\partial x} \tag{5}$$

$$q_z = -k\frac{\partial T}{\partial z} \tag{6}$$

$$H_s = \sigma'_{ij}\dot{\varepsilon}'_{ij,vp} \tag{7}$$

$$H_a = T\alpha_\rho\left(v_x\frac{\partial P}{\partial x} + v_z\frac{\partial P}{\partial z}\right) \tag{8}$$

where k is thermal conductivity, $\dot{\varepsilon}'_{ij,vp}$ is the visco-plastic component of the deviatoric strain rate tensor, and α is the thermal expansion coefficient. H_r is constant for each rock type (Table S1). A constitutive equation (Eq. 9) relates visco-elasto-plastic deviatoric stresses and strain rates $\dot{\varepsilon}'_{ij}$ by applying linear elasticity and non-Newtonian viscosity (Gerya & Yuen, 2007):

$$\dot{\varepsilon}'_{ij} = \frac{1}{2\eta}\sigma'_{ij} + \frac{1}{2G}\frac{D\sigma'_{ij}}{Dt} + \begin{cases} 0 & \text{if} \quad \sigma'_{\mathrm{II}} < \sigma_{\mathrm{yield}} \\ \chi\frac{\partial G_{pl}}{\partial \sigma'_{II}} & \text{if} \quad \sigma'_{\mathrm{II}} = \sigma_{\mathrm{yield}}. \end{cases} \tag{9}$$

where η is the effective viscosity, G is the shear modulus, $\frac{D\sigma'_{ij}}{Dt}$ is the objective co-rotational time derivative solved using a time explicit scheme, χ is a plastic multiplier connecting plastic strain rates and stresses, $\sigma'_{II} = \sqrt{\sigma'^2_{xx} + \sigma'^2_{xz}}$ is the second invariant of the stress tensor, and σ_{yield} is the local plastic yield strength.

Plastic failure is simulated with the Drucker-Prager plastic yielding criterion. At each Lagrangian marker, yielding occurs when the second invariant of the deviatoric stress tensor σ'_{II} reaches the local plastic yield strength σ_{yield} defined as

$$\sigma_{yield} = C + \mu_s(1 - \lambda)P \tag{10}$$

where C is cohesion, μ_s is a constant static friction coefficient, P is pressure, and λ is the pore-fluid pressure factor (P_{fluid}/P).

Text S2. Model setup. The model setup (see Fig. 1) is similar to Brizzi, van Zelst, Funiciello, Corbi, and van Dinther (2020). It consists of oceanic lithosphere that subducts beneath continental lithosphere. The oceanic lithosphere includes a sedimentary layer of variable thickness d_{sed} that is varied between 0 km (no sediments) and 6 km. The sediment layer is designed to deliver a constant sediment flux to the subduction zone. The model setup also includes an initial sedimentary wedge at the leading edge of the overriding plate. Sediments can therefore be transported to depth along the subduction interface and/or added to the front and base of the pre-existing wedge. The computational domain is 1900 × 660 km^2 (1831 × 362 nodes). The grid size is 500 m in the high resolution area around the megathrust and increases to 2000 m at the edges of the models. Lithological structure is resolved with ~33 million markers.

We use a 12.5 km thick layer of sticky air ($\eta_{air} = 10^{18}$ Pa s, $\rho_{air} = 1$ kg/m^3) to mimic the effect of a free surface and enable the development of topography (Crameri et al., 2012). Free slip boundary conditions are applied at the top and side boundaries of the model, and we impose a closed boundary condition at the bottom boundary.

The initial thermal structure of the oceanic lithosphere is calculated from the half-space cooling model (Turcotte & Schubert, 2002) for a 40 Myr old slab and a diffusivity of 10^-6 m^2s-1. The initial temperature of the continental lithosphere linearly increases from T = 0 °C at the surface to T = 1300 °C at 100 km depth. The thermal gradient of the asthenospheric mantle is adiabatic and set to 0.5°C/km.

Subduction initiates along a 15°-dipping weak zone with low plastic strength (1 MPa) and wet olivine rheology (Ranalli, 1995). We impose a constant velocity of 7.5 cm/yr within a small region of the subducting plate (see Fig. 1) until 300 km of the slab is subducted into the mantle. This corresponds to 4 Myr of subduction. After this kinematically prescribed phase, the pushing velocity is removed, and subduction is self-driven.

Text S3. Estimation of the percentage of accreted and subducted sediments. To estimate how sediments are partitioned between the accretionary wedge and the subduction channel, we use compositional maps. At each time step, we contour all sediment rock types (i.e., incoming plate and pre-existing wedge) starting from the trench (Fig. S1a). We then compute the area of this contour polygon, which is a measure of the total amount of sediments. We then discriminate between sediments that are above and below the continental Moho (∼40 km depth). The amount of subducted sediments d_{ss} is computed as the area of sediments below the continental Moho (Fig. S1b). To estimate the amount of accreted sediments, we consider the area of sediments above the continental Moho and we identify the pre-existing wedge sediments (Fig. S1c). The amount of accreted sediments is computed as the difference between the area of sediments above the continental Moho and the area of the pre-existing wedge sediments (Fig S1d). The percentages of accreted and subducted sediments are computed considering the area of the total amount of sediments.

Flow law[a]	ρ_0^b $(kg\,m^{-3})$	E_a^a $(kJ\,mol^{-1})$	V_a^a $(J\,bar^{-1})$	n[a]	η_0^a $(Pa^n\,s)$	H_r^b $(\mu W\,m^{-3})$	k[a] $(Wm^{-1}k^{-1})$	G (GPa)	$\mu_s^{c,d,e}$	λ
Sediments (Wet Qz)	2800[g]	154	0.8	2.3	$1.97 \cdot 10^{17}$	2	$[0.64+807/(T+77)]\ \exp(4 \cdot 10^{-6}P)$	5	0.35	0.95[f]
Upper cont. crust (Wet Qz)	2700	154	1.2	2.3	$1.97 \cdot 10^{17}$	1	$[0.64+807/(T+77)]\ \exp(4 \cdot 10^{-6}P)$	12	0.72	0.4
Lower cont. crust (Wet Qz)	2700	154	1.2	2.3	$1.97 \cdot 10^{21}$	1	$[0.64+807/(T+77)]\ \exp(4 \cdot 10^{-6}P)$	12	0.72	0.4
Upper oc. crust (Wet Qz)	3000	154	0.8	2.3	$1.97 \cdot 10^{17}$	0.25	$[1.18+974/(T+77)]\ \exp(4 \cdot 10^{-6}P)$	12	0.5	0.4
Lower oc. crust (Plg-An 75%)	3000	238	0.8	3.2	$4.8 \cdot 10^{22}$	0.25	$[1.18+974/(T+77)]\ \exp(4 \cdot 10^{-6}P)$	12	0.85	0.4
Mantle (Dry Olivine)	3300	532	0.8	3.5	$3.98 \cdot 10^{16}$	0.0022	$[0.73+1293/(T+77)]\ \exp(4 \cdot 10^{-6}P)$	35	0.6	0.4

Table S1. Rheological parameters. ρ_0 is the reference density, E_a is the activation energy, V_a is the activation volume, n is the stress exponent, η_0 is the reference viscosity, H_r is the radiogenic heat production, G is the shear modulus, μ_s is the static friction coefficient and λ is the pore-fluid pressure factor (P_{fluid}/P_{solid}). Other properties for all rock types: cohesion (C) is 6 MPa (Schultz, 1995), specific heat capacity (C_p) is 1000 $Jkg^{-1}K^{-1}$, thermal conductivity (k) is in $Wm^{-1}k^{-1}$ at T_K and P_{MPa}, thermal expansion α_ρ = 3x10^{-5} K^{-1} and compressibility β_ρ = 1x10^{-3} MPa^{-1}. [a]Ranalli (1995); [b]Turcotte and Schubert (2002); [c]Di Toro et al. (2011); [d] Del Gaudio et al. (2009); [e]Den Hartog et al. (2012); [f]Seno (2009). [g]In a second set of models, sediment density was set to 2200 kg/m^3 and 2600 kg/m^3.

References

Brizzi, S., van Zelst, I., Funiciello, F., Corbi, F., & van Dinther, Y. (2020). How Sediment Thickness Influences Subduction Dynamics and Seismicity. *Journal of Geophysical Research: Solid Earth*, *125*(8), 1–19. doi: 10.1029/2019JB018964

Crameri, F., Schmeling, H., Golabek, G., Duretz, T., Orendt, R., Buiter, S., . . . Tackley, P. (2012). A comparison of numerical surface topography calculations in geodynamic modelling: an evaluation of the 'sticky air'method. *Geophysical Journal International*, *189*(1), 38–54.

Del Gaudio, P., Di Toro, G., Han, R., Hirose, T., Nielsen, S., Shimamoto, T., & Cavallo, A. (2009). Frictional melting of peridotite and seismic slip. *Journal of Geophysical Research: Solid Earth*, *114*(B6).

Den Hartog, S. A. M., Niemeijer, A. R., & Spiers, C. J. (2012). New constraints on megathrust slip stability under subduction zone P–T conditions. *Earth and Planetary Science Letters*, *353*, 240–252.

Di Toro, G., Han, R., Hirose, T., De Paola, N., Nielsen, S., Mizoguchi, K., . . . Shimamoto, T. (2011). Fault lubrication during earthquakes. *Nature*, *471*(7339), 494.

Gerya, T. V., & Yuen, D. A. (2007). Robust characteristics method for modelling multiphase visco-elasto-plastic thermo-mechanical problems. *Physics of the Earth and Planetary Interiors*, *163*(1-4), 83–105. doi: 10.1016/j.pepi.2007.04.015

Ranalli, G. (1995). *Rheology of the earth.* Springer Science & Business Media.

Seno, T. (2009). Determination of the pore fluid pressure ratio at seismogenic megathrusts in subduction zones: Implications for strength of asperities and Andean-type mountain building. *Journal of Geophysical Research: Solid Earth*, *114* (5), 1–25. doi: 10.1029/2008JB005889

Turcotte, D. L., & Schubert, G. (2002). *Geodynamics.* Cambridge university press.

van Dinther, Y., Gerya, T. V., Dalguer, L. A., Mai, P. M., Morra, G., & Giardini, D. (2013, dec). The seismic cycle at subduction thrusts: Insights from seismo-thermo-mechanical models. *Journal of Geophysical Research: Solid Earth*, *118* (12), 6183–6202. doi: 10.1002/2013JB010380

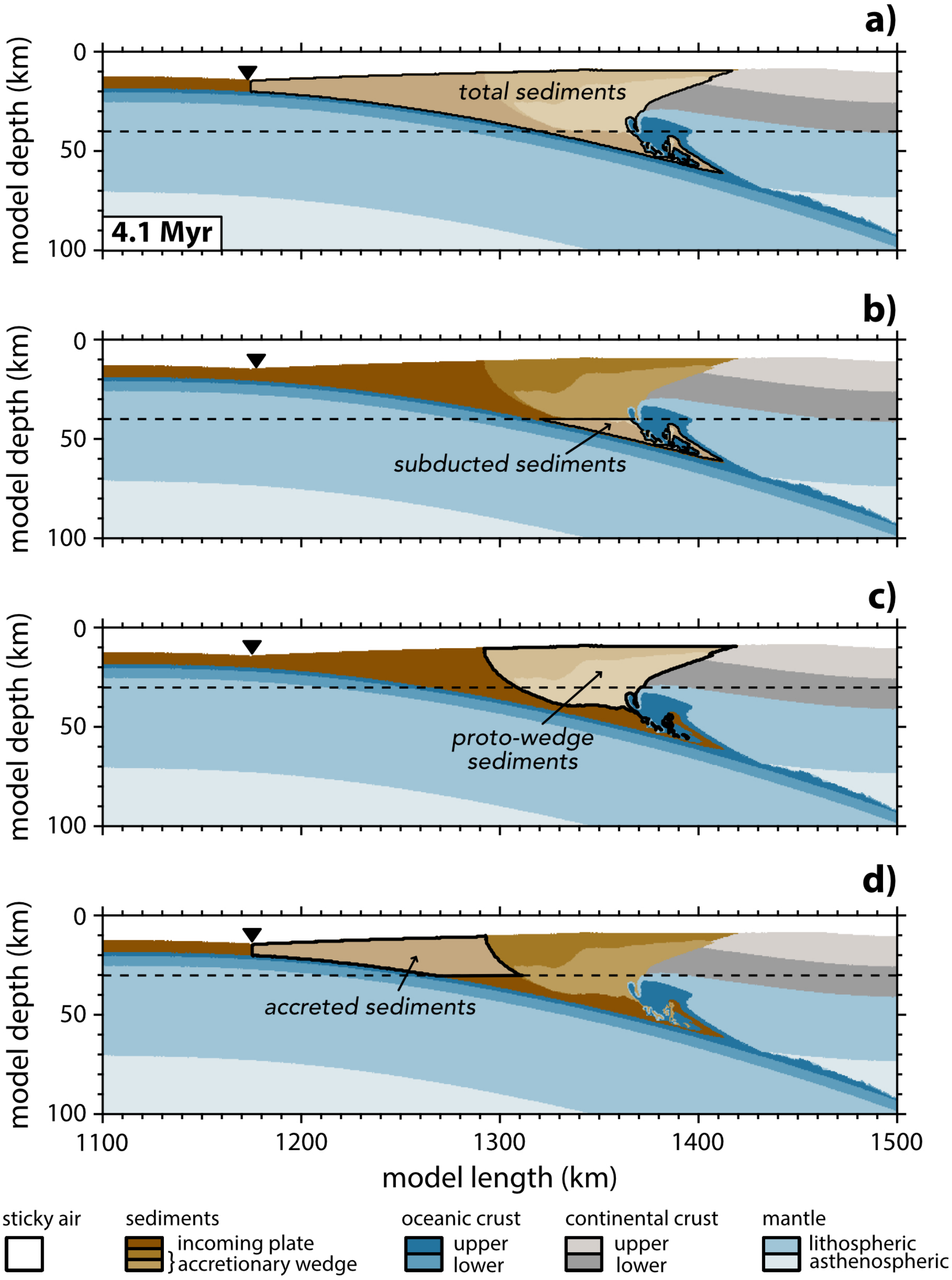

Figure S1. Compositional map of the model with a thick sedimentary layer (d_{sed} = 6 km and ρ_{sed} = 2800 kg/m^3) at ∼4.1 Myr. a) Total sediments, b) subducted sediments, c) pre-existing wedge sediments, and d) accreted sediments. The black dashed line marks the approximate depth of the continental Moho. The black triangle marks the location of the trench.

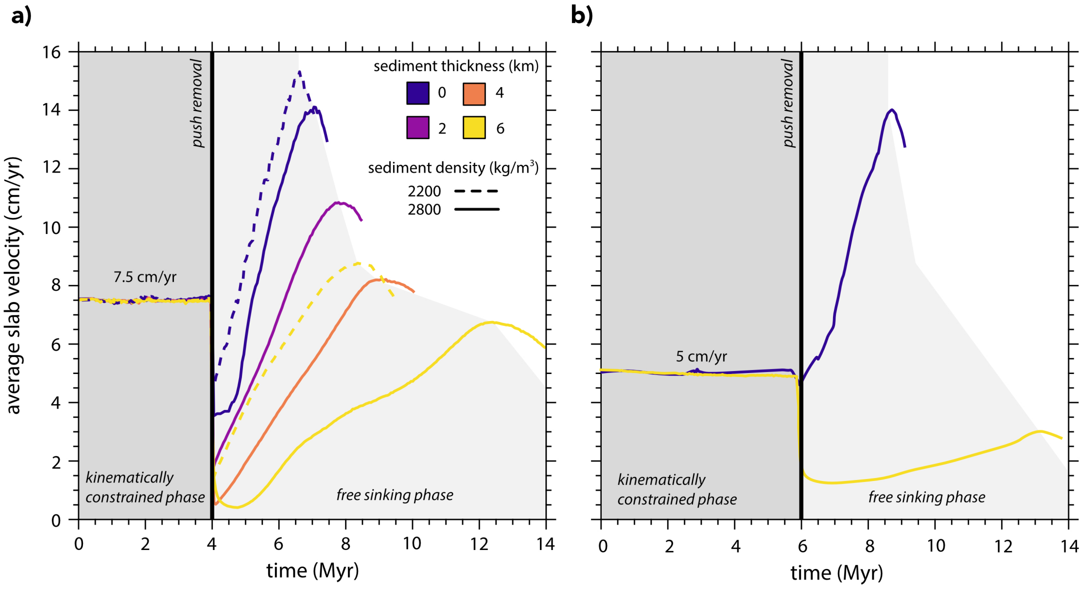

Figure S2. a) Slab velocity through time for models with different sediment thickness d_{sed} and density ρ_{sed}. The push velocity is 7.5 cm/yr. The black line marks the timing of the push removal. The slab velocity v_{sp} as the average velocity of the slab during the free sinking phase (light gray shaded area). b) Slab velocity as a function of time for two end-member models (d_{sed} = 0 km and 6 km, ρ_{sed} = 2800 kg/m^3) with a 5 cm/yr push velocity.

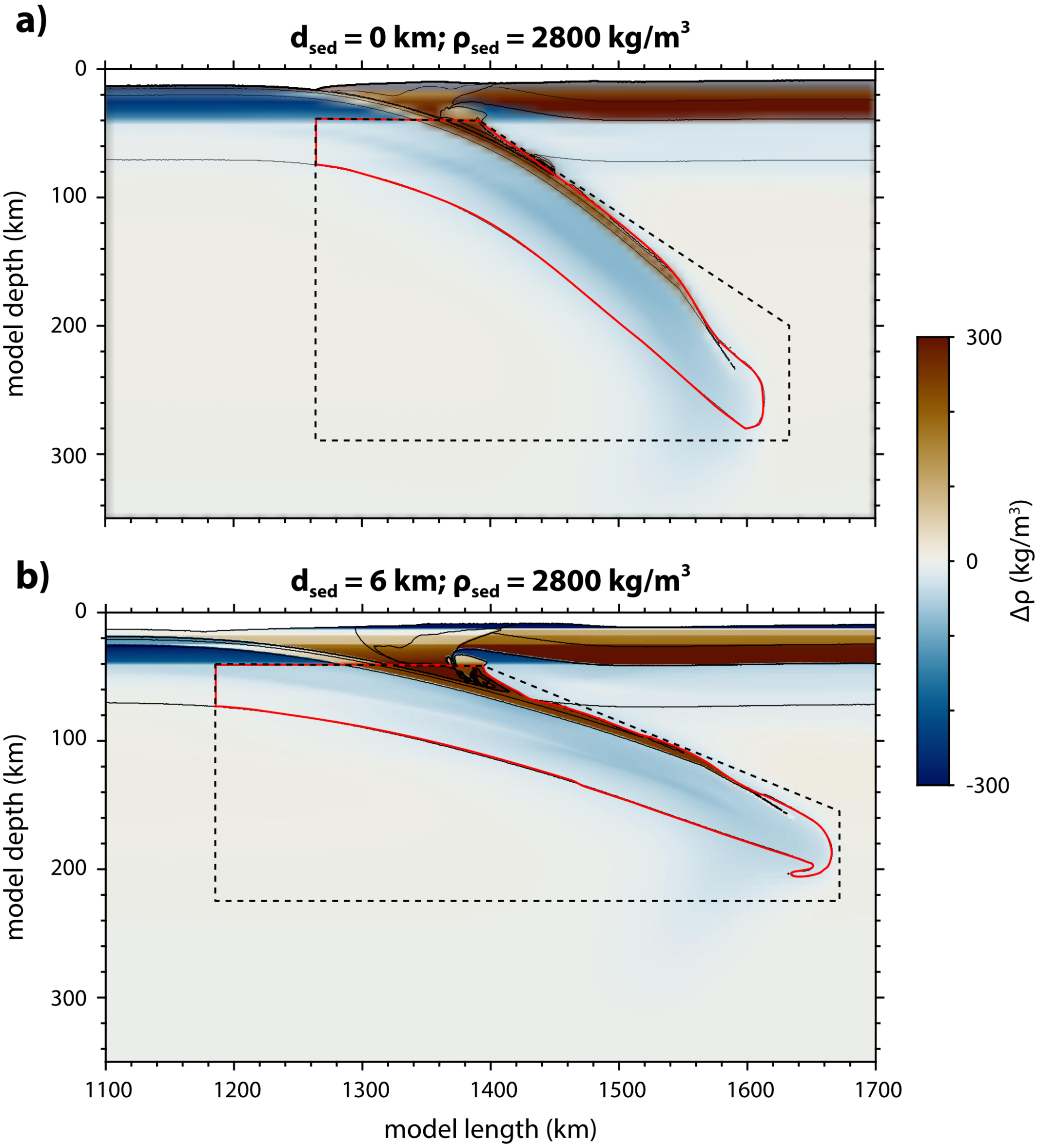

Figure S3. Density contrast $\Delta\rho$ between the asthenospheric mantle and the slab for the model with a) thin (d_{sed} = 0 km) and b) thick (d_{sed} = 6 km) sediment layer, and sediment density ρ_{sed} = 2800 kg/m^3 at ∼4 Myr (when the push velocity is removed). $\Delta\rho$ is computed as the difference between the horizontal average of density and the local density. The dashed black polygon depicts the trapezoidal region within which $\Delta\rho$ is averaged to compute slab pull. The red polygon is the slab area A.

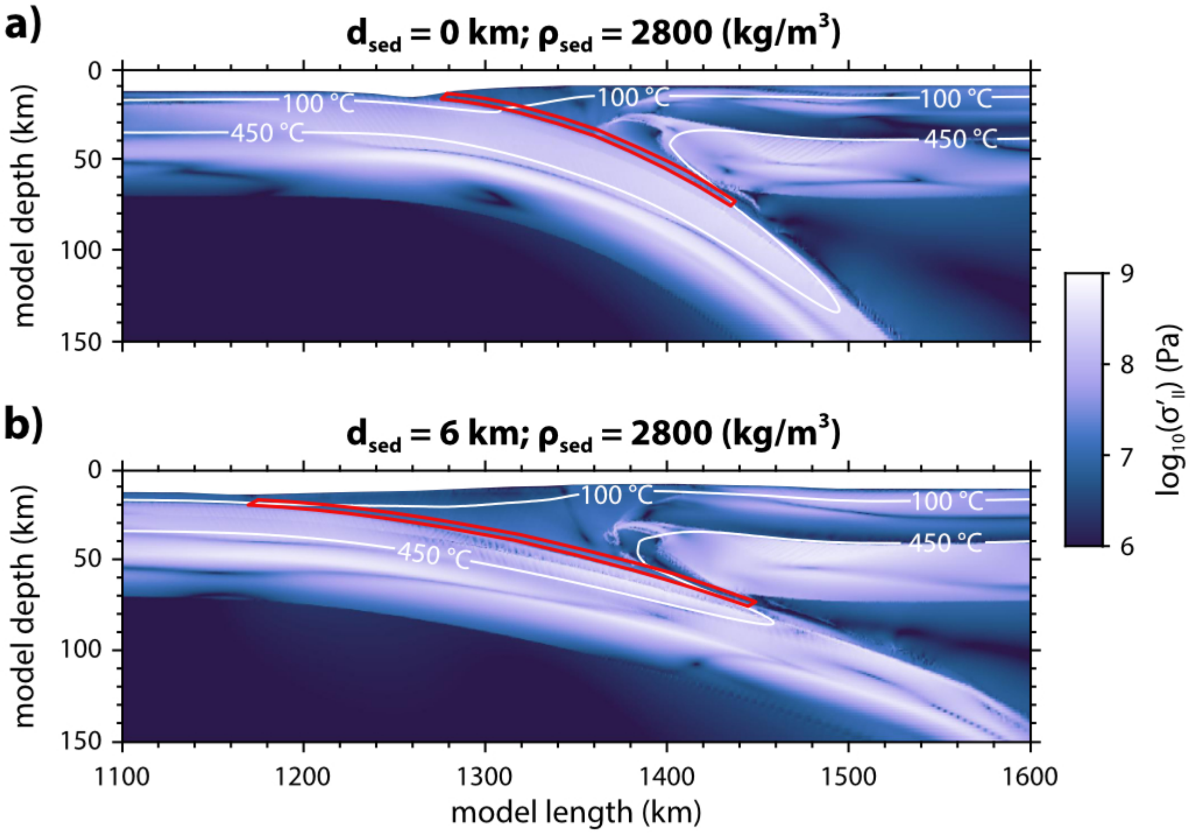

Figure S4. Second invariant of the deviatoric stress tensor $\sigma'_{||}$ for the model with a) thin ($d_{sed} = 0$ km) and b) thick ($d_{sed} = 6$ km) sedimentary layer, and sediment density $\rho_{sed} = 2800$ kg/m^3 at ∼4 Myr (when the push velocity is removed). The integrated megathrust shear stress F_{sl} is computed as the sum of $\sigma'_{||}$ within a 3 km-wide polygon that extends from the trench to the 450 °C isotherm (red rectangle) times the length of the polygon. For simplicity, the length of the polygon is approximated to a straight line.

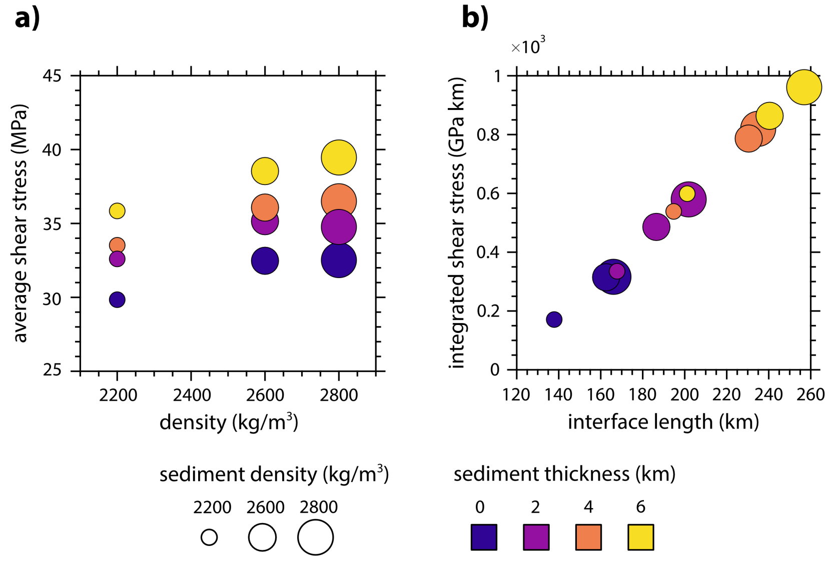

Figure S5. a) Average shear stress of the plate interface as a function of sediment thickness d_{sed} and density ρ_{sed}. The average shear stress is the average of the second invariant of the deviatoric stress tensor $\sigma'_{||}$ in a 3 km wide region that extends from the trench to the 450 °C isotherm (see also Fig. S4). b) Relationship between integrated shear stress of the megathrust F_{sl} and interface length for models with different sediment thickness d_{sed} and density ρ_{sed}.